

# Constraints on Large-Scale Magnetic Fields in the Intergalactic Medium Using Cross-Correlation Methods

A.D. Amaral,<sup>1,2</sup>\* T. Vernstrom,<sup>2,3</sup> and B.M. Gaensler<sup>2,1</sup>

<sup>1</sup>David A. Dunlap Department of Astronomy and Astrophysics, University of Toronto, ON, M5S 3H4, Canada

<sup>2</sup>Dunlap Institute for Astronomy and Astrophysics, University of Toronto, Toronto, ON, M5S 3H4, Canada

<sup>3</sup>CSIRO Astronomy and Space Science, PO Box 1130, Bentley, WA 6102, Australia

Accepted XXX. Received YYY; in original form ZZZ

## ABSTRACT

Large-scale coherent magnetic fields in the intergalactic medium are presumed to play a key role in the formation and evolution of the cosmic web, and in large scale feedback mechanisms. However, they are theorized to be extremely weak, in the nano-Gauss regime. To search for a statistical signature of these weak magnetic fields we perform a cross-correlation between the Faraday rotation measures of 1742 radio galaxies at  $z > 0.5$  and large-scale structure at  $0.1 < z < 0.5$ , as traced by 18 million optical and infrared foreground galaxies. No significant correlation signal was detected within the uncertainty limits. We are able to determine model-dependent  $3\sigma$  upper limits on the parallel component of the mean magnetic field strength of filaments in the intergalactic medium of  $\sim 30$  nG for coherence scales between 1 and 2.5 Mpc, corresponding to a mean upper bound RM enhancement of  $\sim 3.8$  rad/m<sup>2</sup> due to filaments along all probed sight-lines. These upper bounds are consistent with upper bounds found previously using other techniques. Our method can be used to further constrain intergalactic magnetic fields with upcoming future radio polarization surveys.

**Key words:** magnetic fields – intergalactic medium: intergalactic filaments – large-scale structure of the universe – methods: statistical – radio continuum: galaxies

## 1 INTRODUCTION

Astronomers have been able to detect the presence of magnetic fields across many scales, both Galactic and extra-galactic (see Vallée 1997, 1998, 2004 for reviews). However, magnetic fields on the largest scales in the Universe remain largely unconstrained (Widrow 2002). These scales are occupied by filaments, voids, and galaxy clusters, where over-dense filaments connect to form the Universe’s large-scale structure known as the cosmic web (Springel et al. 2006).

The dominant gas phase of filaments is in the form of the warm hot ionized medium (WHIM), which contains baryons at high temperatures ( $10^5\text{K} \leq T \leq 10^7\text{K}$ , Ryu et al. 2008) due to shock heating. At low redshifts, the WHIM is thought to contain  $\sim 40\%$  of the intergalactic medium (IGM) and the majority of the baryons in the Universe, making it an important component of the Universe to understand (Cen & Ostriker 1999, 2006; Dolag et al. 2006; Davé et al. 2010). These IGM filaments play a vital role in intergalactic gas feedback processes by providing pristine gases and elements to galaxies to fuel star formation via cold streams (Man & Belli 2018). Any large-scale magnetic fields present in filaments would likely have an effect on this process (Klar & Mücke

2012). Moreover, most theories that explain how magnetic fields in galaxies form and evolve over cosmic time (such as the  $\alpha - \Omega$  dynamo, see Kulsrud & Zweibel 2008 for a review) require the presence of an initial weak seed field within the IGM at early times.

It is certain that magnetic fields existed on small-scales in the primordial Universe, due to the presence of currents, though their presence on larger cosmic scales remains theoretical (Grasso & Rubinstein 2001). These primordial magnetic fields (PMFs) may have been generated during early phase transitions along phase bubbles (such as the quantum chromodynamic and electroweak phase transitions, Widrow 2002), or shocks present during these transitional phase boundaries could have amplified and generated magnetic fields with coherence scales on the order of the phase bubbles (Kahniashvili et al. 2013). Big bang nucleosynthesis chemical abundances place bounds on PMFs from nG to  $\mu\text{G}$  (Grasso & Rubinstein 1995; Cheng et al. 1996; Kawasaki & Kusakabe 2012). Bounds on the presence of PMFs from the temperature and polarization maps of the cosmic microwave background (CMB) are  $\leq 10$  nG (Planck Collaboration et al. 2016b). Cosmic-scale magnetic fields also may have been seeded from astrophysical sources that release large amounts of magnetic flux into the IGM. Examples of such sources include the highly magnetized coherent outflows from active galactic nuclei (AGN),

\*E-mail: amaral@astro.utoronto.ca

which contain charged particles undergoing acceleration in jets (Furlanetto & Loeb 2001). The strength of the outflows can stretch magnetic field lines, causing large coherence scales and spreading outwards into the IGM (Furlanetto & Loeb 2001). In a similar manner, the first starburst galaxies could have generated significant magnetized winds due to rapid star formation, injecting magnetic flux into the surrounding IGM (Kronberg et al. 1999).

The presence of magnetic fields have been inferred observationally for galaxies at high redshifts (Kronberg & Perry 1982; Wolfe et al. 1992; Oren & Wolfe 1995; Bernet et al. 2008; Mao et al. 2017), indicating that generation mechanisms must be present in the early universe. Additionally, large-scale  $\mu\text{G}$  fields have been detected in the intra-cluster medium (ICM) between galaxies (Kim et al. 1991; Feretti et al. 1995; Clarke et al. 2001; Bonafede et al. 2010, 2013), and in galaxy cluster haloes on the outskirts of the ICM (Roland 1981; Kim et al. 1990).

The difficulty detecting intergalactic magnetic fields (IGMFs) is due to the fact that these fields are theorized to be extremely weak, in the nG regime, and contain magnetic field reversals (Ryu et al. 2008; Cho & Ryu 2009; Akahori & Ryu 2010; Vazza et al. 2015b; Akahori et al. 2016). Additionally, the density of relativistic particles is low in these environments (Cen & Ostriker 2006; Bregman 2007), making detection via synchrotron emission difficult (Brown 2011; Vazza et al. 2015a).

Direct detections of IGMFs may only be possible through data from future telescopes (such as the upcoming Square Kilometre Array and its pathfinders, Gaensler 2009). Until then, statistical and indirect methods must be used in order to infer their presence. Measured properties from these techniques, such as the field strength and coherence scale, can differentiate between magnetogenesis models (Donnert et al. 2009; Vacca et al. 2015). Statistical methods using Faraday rotation data can be used to place upper bounds on line-of-sight magnetic fields permeating the IGM. Magneto-ionic media are birefringent, thus as linearly polarized light pass through magnetic fields it undergoes Faraday rotation, in which the polarization angle of the radiation rotates along the line-of-sight. The degree of observed rotation is:

$$\Delta\Phi = RM\lambda^2, \quad (1)$$

where  $\lambda$  is the observed wavelength, and RM is a proportionality constant called the rotation measure. This RM can be used to infer information about the line-of-sight component of the magnetic fields causing the Faraday rotation. The RM is given by:

$$RM = 812 \int_{z_s}^0 (1+z)^{-2} n_e(z) B_{\parallel}(z) dz \cdot \frac{dl}{dz} \text{ rad m}^{-2}, \quad (2)$$

where  $z_s$  is the redshift of the emitting polarized source,  $n_e$  is the column density of free electrons along the line-of-sight to the source measured in  $\text{cm}^{-3}$ ,  $B_{\parallel}$  is the line-of-sight component of the magnetic field measured in  $\mu\text{G}$ , and the line-of-sight  $dl$  is measured in kpc.

Because the RM is an integrated effect along the line-of-sight from a distant source towards Earth, it contains the rotation measure induced within the source itself ( $\text{RM}_{\text{intrinsic}}$ ), an intervening extra-galactic component ( $\text{RM}_{\text{intervening}}$ ), a Galactic component ( $\text{RM}_{\text{Galactic}}$ ), and a component due to noise ( $\text{RM}_{\text{noise}}$ ):

$$RM = \text{RM}_{\text{intrinsic}} + \text{RM}_{\text{intervening}} + \text{RM}_{\text{Galactic}} + \text{RM}_{\text{noise}}. \quad (3)$$

Various statistical methods have been applied to place upper

bounds on large-scale IGMFs, such as quantifying RM growth over redshift for large samples (Blasi et al. 1999; Kronberg et al. 2008; Bernet et al. 2013; Hammond et al. 2012; Xu & Han 2014; Pshirkov et al. 2016; Neronov et al. 2013), and quantifying RM differences between physical pairs vs. sources that are close on the sky but occupy different redshifts (Vernstrom et al. 2019). In cases where redshift information is unavailable, studies looked at non-physical pairs assuming that  $z$  would not be identical (O’Sullivan et al. 2020; Stuardi et al. 2020). These techniques have placed upper bounds on IGMFs ranging from  $\sim \text{nG}$  to  $\sim \mu\text{G}$ , depending on the method and assumptions used.

### 1.1 Cross-correlation techniques

Cross-correlation techniques between extragalactic RM-grids (regions of sky with large numbers of RM measurements) and tracers of large-scale structure can be used as another method to extract the IGMF signal. Because it is difficult to directly observe large scale structure, wide-field galaxy catalogues and galaxy number density grids can be used to trace large-scale structure and the corresponding IGM. This has been done with success using various wide field multi-wavelength galaxy catalogues (see Jarrett 2004, or Gilli et al. 2003 for examples). If large-scale magnetic fields exist within the IGM as traced by galaxy densities, any polarized sources behind this IGMF will have an intervening RM contribution due to this magnetic field, as described in equation 3. If the background RMs are correlated with the foreground galaxy densities on large scales, this suggests the presence of a large-scale magnetic field within the IGM.

A cross-correlation technique was used on mock foreground-subtracted extragalactic RM catalogues by Kolatt (1998) to detect features of a PMF power spectrum. Xu et al. (2006) cross correlated RMs in galaxy superclusters (such as Hercules, Virgo, and Perseus), with galaxy densities of the clusters to search for a signal from the IGMF within these structures; they found an upper limit of  $\sim 0.3 \mu\text{G}$  for coherence scales of 500 kpc.

More recently, Lee et al. (2009) used a cross-correlation technique over large regions of the sky ( $120^\circ < \alpha < 240^\circ$ ,  $0^\circ < \delta < 60^\circ$ ) between 7244 extragalactic RMs from Taylor et al. (2009) catalogue, and the sixth data release of the Sloan Digital Sky Survey (SDSS) with photometric redshifts (Oyaizu et al. 2008) to trace large-scale structure. They found a positive correlation between the two quantities at large-scales, indicating a field strength of  $\sim 30 \text{ nG}$ . However, Lee et al. (2010) withdrew this result because the cross-correlation was found to be spurious. This points to the prospect of detecting such signals, but also demonstrates that the interpretation can be susceptible to statistical errors. This claimed result and its subsequent retraction motivates our study: we here revisit this technique, but with a more careful and thorough approach to systematics and uncertainties.

Some work has been done on what such cross-correlations would look like for large data-sets of simulated RMs of various large scale IGMF strengths, and using galaxy catalogues as tracers for structures on large-scales (such as by Staszyszyn et al. 2010 and Akahori et al. 2014). Given sufficient sample sizes, one can discern between magneto-genesis models given the shape and amplitude of the cross-correlation.

In this work, we place upper bounds on the IGMF by using cross-correlation techniques between the largest RM-redshift catalogue currently available, and an all-sky galaxy catalogue with photometric redshifts. The paper is organized as follows; in Section 2 we describe the methods used to constrain the IGMF signal; in

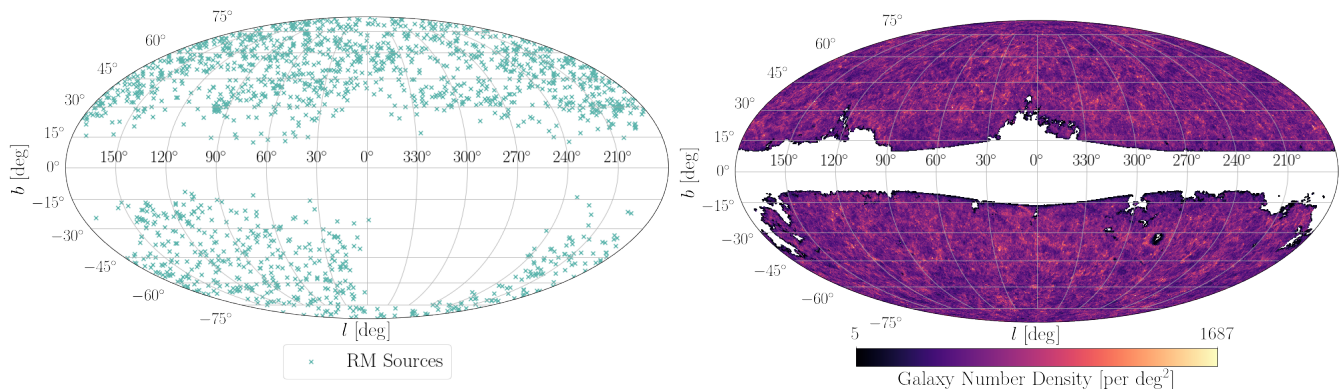


**Figure 1.** **Left:** Locations of 1742 background RM sources from [Hammond et al. \(2012\)](#) after making selection cuts described in Section 3.1. **Right:** Distribution of 18 million foreground galaxies ( $0.1 < z < 0.5$ ) from WISExSuperCOSMOS.

Section 3 we discuss the data used in our analysis; in Section 4 we present the cross-correlation and its results; and in Section 5 we place corresponding upper limits on the magnetic field of the IGM, and discuss how future work with upcoming surveys can improve constraints on large-scale magnetic fields in the IGM. Throughout the paper we assume a  $\Lambda$ CDM cosmology of  $H_0 = 67.8 \text{ km s}^{-1} \text{ Mpc}^{-1}$  and  $\Omega_M = 0.308$  ([Planck Collaboration et al. 2016a](#)).

## 2 DATA

### 2.1 Rotation Measure Catalogue

We use the [Taylor et al. \(2009\)](#) RM catalogue, which derived RMs from the NRAO VLA Sky Survey (NVSS, [Condon et al. 1998](#)). The NVSS contains images of Stokes I, Q, U, at 1.4 GHz, at 45 arcsecond resolution for 1.8 million sources at declinations greater than  $\delta > -40^\circ$ . [Taylor et al. \(2009\)](#) then reprocessed the original NVSS data to determine RMs for 37 543 radio sources with signal-to-noise ratios greater than  $8\sigma$ , using two frequency bands centred at 1364.9 MHz and 1435.1 MHz. Given that only two narrowly spaced frequency bands were used to determine the RMs, the values derived might be prone to errors (such as the  $n\pi$  ambiguity; see Section 3.4.2 for further discussion). This is currently still the largest single catalogue of rotation measures to date. For our work, the RM sources must be at large redshifts such that their radiation passes through the foreground galaxies that trace large-scale structure. To determine if a source is a background source, the redshift is needed - this information is not available in [Taylor et al. \(2009\)](#). [Hammond et al. \(2012\)](#) cross-matched the [Taylor et al. \(2009\)](#) catalog with optical surveys and online databases (such as SDSS DR8; [Aihara et al. 2011](#)), and databases, such as SIMBAD ([Wenger et al. 2000](#))<sup>1</sup> and NED<sup>2</sup>, to obtain spectroscopic redshifts. This yields a sample of 4003 sources with RMs and spectroscopic redshifts, which allows us to ensure that the RM sources are indeed background sources, or at higher redshifts, than the galaxies (see Section 2.2) for cross-correlating.

<sup>1</sup> <http://simbad.u-strasbg.fr/simbad/>

<sup>2</sup> The NASA/IPAC Extragalactic Database (NED) is funded by the National Aeronautics and Space Administration and operated by the California Institute of Technology. More information can be found at: <https://ned.ipac.caltech.edu>

The left panel in Figure 1 shows the sky distribution of RMs used for this study.

### 2.2 Galaxy Catalogue

We use the WISExSuperCOSMOS ([Bilicki et al. 2016](#)) survey as our tracer for foreground large-scale structure. This catalogue is the product of cross-matching between the mid-IR Wide-field Infrared Survey Explorer (WISE, [Wright et al. 2010](#)) and the optical SuperCOSMOS ([Hambly et al. 2001](#)) all-sky surveys, and contains 20 million cross-matched galaxies after filtering for quasars and stars and other tests. To generate accurate photometric redshifts, [Bilicki et al. \(2016\)](#) cross-matched their WISExSuperCOSMOS catalogue with the Galaxy and Mass Assembly-II (GAMA-II) survey ([Driver et al. 2009](#)), an extragalactic (clean from stars and quasars) spectroscopic survey that includes 193,500 overlapping sources with WISExSuperCOSMOS. They used this as a training set for the ANNz package, an artificial neural network package that assigns photometric redshifts to a sample given a training set with both photometric and spectroscopic redshifts. [Bilicki et al. \(2016\)](#) were thus able to determine photometric redshifts for all 20 million sources.

We require redshifts for the galaxies to ensure that they are indeed foreground to the RM sources discussed in Section 2.1. The WISExSuperCOSMOS catalogue was used due to the fact that it provides redshifts necessary for this study (with a median galaxy redshift  $z \approx 0.2$ ). Compared to other galaxy surveys, WISExSuperCOSMOS also has many sources and covers at least 70% of the sky, allowing for a good tracer of large-scale structure. The right panel of Fig. 1 shows the galaxy density distribution used for this study.

## 3 CROSS-CORRELATION ANALYSIS

### 3.1 Sample Selection

To cross-correlate between RMs and large-scale structure, we must ensure that the polarized radio sources are background sources whose radiation pass through the IGM of the large-scale structure traced by foreground galaxies. The redshift distribution of the WISE galaxies severely drops off for  $z > 0.5$  as shown in Figure 2a. Thus we set  $z = 0.5$  as the redshift limit; defining RM sources with  $z < 0.5$  as foreground and  $z \geq 0.5$  as background sources. [Bilicki et al. \(2016\)](#) found that the photometric redshifts

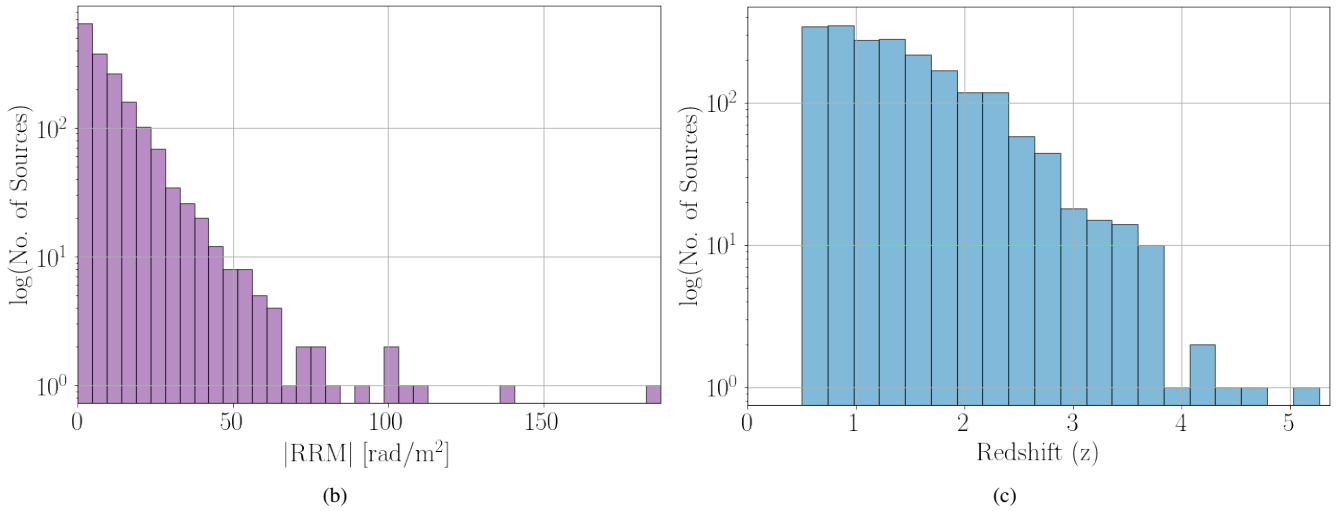
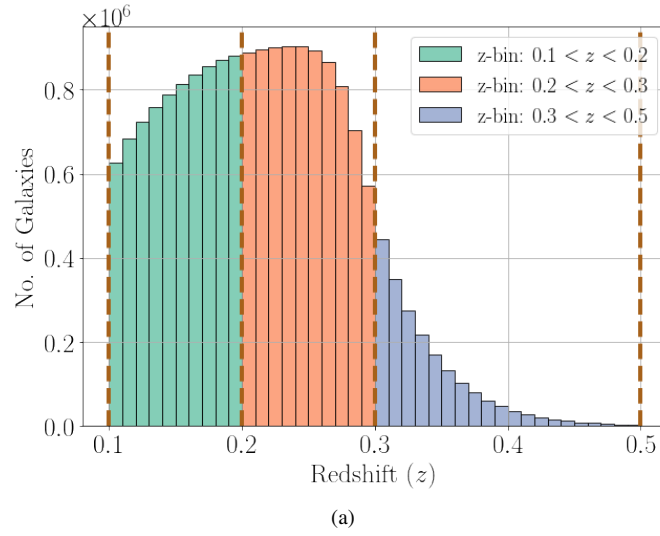


**Figure 2.** The distributions of the polarized background RM sources, and the foreground galaxies used in the cross-correlation: **(a)** The redshift distribution of the galaxies used in this study from WISExSuperCOSMOS. **(b)** The  $|RRM|$  distribution of the RM sources used, and **(c)** The redshift distribution of the RM sources used.

of the galaxy catalogue for galaxies with  $z < 0.1$  contained higher fractional errors and contamination of foreground stars. We thus require galaxies to have redshifts between  $0.1 < z < 0.5$ , leaving 18, 189, 238 foreground galaxies.

Due to uncertainties associated with photometric redshifts of the foreground galaxies, we choose to use redshift bins of widths of  $\Delta z = 0.1$  for the first two redshift bins (as recommended by Bilicki et al. 2016) and  $\Delta z = 0.2$  for the final redshift bin for our analysis. To ensure a large enough number of sources in each bin, we chose to bin the galaxies in the following manner:  $0.1 < z < 0.2$  (containing 7, 840, 929 galaxies),  $0.2 < z < 0.3$  (containing 8, 336, 519), and  $0.3 < z < 0.5$  (containing 2, 011, 790 galaxies). There is a total of 18, 189, 238 galaxies across all three redshift bins. The mean redshift of the galaxies in each bin is:  $z_{\text{mean}} = 0.15, 0.247, \text{ and } 0.34$ , respectively.

We use a HEALPix<sup>3</sup> (Górski et al. 2005) gridding scheme and

healpy<sup>4</sup> (Zonca et al. 2019) to split-up the all-sky foreground galaxies into a number density grid using spherical projection pixels of equal surface area. We use  $n_{\text{side}} = 128$ , which corresponds to each pixel occupying  $0.21 \text{ deg}^2$  on the sky. The resulting all-sky number density grid of the remaining foreground galaxies can be seen in Figure 1.

Blank cells in the right panel of Figure 1 are due to the presence of the Galactic foreground in the survey coverage, or due to empty grid cells that contain no galaxies. We then removed any RM sources that fell into empty grid cells, and any RM source within 2.5 co-moving Mpc of an empty cell or edge of the WISE galaxy number density map - leaving us with 2229 background RM sources.

Akshori et al. (2016) found that magnetic fields due to galaxy clusters tend to dominate the RM along the line-of-sight, which hence drown out any signal due to weaker magnetic fields, such as those in filaments. Therefore, RMs that intersect cluster sight-lines

<sup>3</sup> <http://healpix.sourceforge.net>

<sup>4</sup> <http://github.com/healpy/healpy/>



correlation are  $|RRM|$ . The  $|RRM|$  distribution of the 1742 background RM sources can be found in Figure 2b, and the corresponding redshift distribution of these sources can be found in Figure 2c. The sky distributions of the RM catalogue and galaxy number density grid after applying our selection criteria are shown in Figure 1.

### 3.3 Cross-Correlation Function

A large-scale magnetic field within the filamentary IGM (as traced by the foreground galaxy distribution) will create an enhanced RM along that line-of-sight (extragalactic component,  $RM_{\text{intervening}}$ , in equation 3) for each polarized background source. Probing impact parameters at various distances from the line-of-sight of the RM source allows us to quantify the extent of influence of the field present in the foreground galaxy field. We wish to probe correlations at large-scales, and thus use 8 linearly spaced radial impact parameter bins extending from the polarized background source between  $\sim 500$  kpc to 2.5 Mpc on the sky. These scales were chosen because the typical thickness of IGM filaments are typically 1-2 Mpc (Ratcliffe et al. 1996; Doroshkevich et al. 2004; Wilcots 2004), therefore we sample 500 kpc on either side of this range. Additionally this choice of radial bin scales ensures that the smoothing scale of the GRMs (see section 3.2) used will not affect the cross-correlation. The GRM smoothing scale does not affect scales smaller than  $\sim 1$  deg (Oppermann et al. 2012), and angular diameter distance for 1 degree (6.9 Mpc at  $z = 0.1$ ) is larger than our largest radial bin of 2.5 Mpc. The coherence scale of the magnetic field is considered to be the scale within which the magnetic field remains uniform with no field reversals. If a signal is observed at a given scale,  $r$ , this suggests that the magnetic field is coherent at this scale. We then can calculate the cross-correlation function,  $\xi(r)$ , between the background RRM and the foreground galaxies using,

$$\xi(r) = \sum_i \sum_j \frac{1}{(1 + \bar{z}_j)^2} \left( \frac{N_{gal,i}(r, z_j) - \langle N_{gal}(r, z_j) \rangle}{A(r)} \right) \cdot (|RRM|_i - \langle |RRM| \rangle). \quad (5)$$

The index  $i$  represents each individual polarized background source with RRM of  $|RRM|_i$ , and index  $j$  represents the 3 redshift bins of the foreground.  $\langle |RRM| \rangle$  is the average residual rotation measure of all of the RRM sources, where  $\langle |RRM| \rangle = 11.1$  rad/m<sup>2</sup>. Here,  $N_{gal,i}(r, z_j)$  is the number of galaxies in redshift bin  $z_j$  and at radial impact distance  $r$  from the line-of-sight of  $RRM_i$ , while  $\langle N_{gal}(r, z_j) \rangle$  is the predicted number of galaxies in each redshift and radial bin around each RRM source. The predicted numbers are determined by assuming a Poisson distribution in each redshift bin and calculating the expected number of sources given the on-the-sky area,  $A(r)$ , of each radial bin,  $r$ . As seen in equation 2, there is a redshift contribution that affects the RM. The foreground galaxies span a substantial redshift range, thus we un-weight this redshift dependence in equation 5 by including the term  $(1 + \bar{z}_j)^{-2}$ , where  $\bar{z}_j$  is the average redshift of that bin.

We are interested in quantifying if any deviations from the average number of galaxies around each RM source correlates with deviations from  $\langle |RRM| \rangle$ . A visual representation of our cross-correlation method can be found in Figure 3.

## 3.4 Results

### 3.4.1 Cross-Correlation of Data

We use equation 5 to calculate the cross-correlation function between background RRM sources and foreground galaxies. The resulting value of  $\xi(r)$  as a function of  $r$  is shown in Figure 4. No strong signal is seen at any value of  $r$ . There is a slight positive signal in the lowest radial bins, with a decreasing trend with increasing  $r$ . In order to determine if any significant detection is made, we determined uncertainties as detailed in the following subsection.

### 3.4.2 Uncertainties

In this section, we calculate the confidence and significance levels of the cross-correlation result from section 3.4.1. We define the confidence levels as the intervals in which we are confident that the resultant cross-correlation falls within, whereas the significance levels define how significant the cross-correlation is above a null signal.

To determine the confidence levels on our cross-correlation result, we use a boot-strap method and randomly re-sample the 1742 RRM sources, with replacement. We do this for 1000 realizations computing a cross-correlation for each realization, then generating  $1\sigma$ ,  $2\sigma$ , and  $3\sigma$  percentiles as the confidence levels on the cross-correlation.

To obtain the significance levels of the cross-correlation, we produce a null cross-correlation signal. To do this, we generate random background radio sources randomly located on the celestial sphere such that the correlation between them and the foreground galaxy density should average to zero in all radial bins. We mask out any values that fall within the Galactic plane ( $-20^\circ < b < 20^\circ$ ).

Using the method described in the preceding paragraphs, we calculate random locations on the celestial sphere for 2,674,800 new sight-lines. From these new locations, we select 1742 and assign each a random RRM from Hammond et al. (2012) catalogue, using bootstrap resampling to form a set of random locations and RRM. We then use these bootstrapped 1742 RRM to compute the cross-correlation function for 1000 different realizations. We then take the  $1\sigma$ ,  $2\sigma$ , and  $3\sigma$  percentiles from the 1000 random cross-correlation realizations to obtain the significance of the result.

The final cross-correlation function can be seen in Figure 4, where the error bars for various confidence levels are plotted in green, and the  $3\sigma$  significance level of the result ( $3\sigma$  confidence level for the null signal) is plotted as red dashed lines.

## 4 DISCUSSION

The cross-correlation between the foreground galaxies and background RM sources (Figure 4) is consistent with zero within  $3\sigma$ . Although no significant signal is detected, the cross-correlation function can still be used to obtain upper limits on the magnetic field of the WHIM within the IGM. We use the significance levels (see Section 3.4.2) on the cross-correlation function determined from the data to constrain an upper bound on the parallel component on large-scale magnetic fields contained in the WHIM.

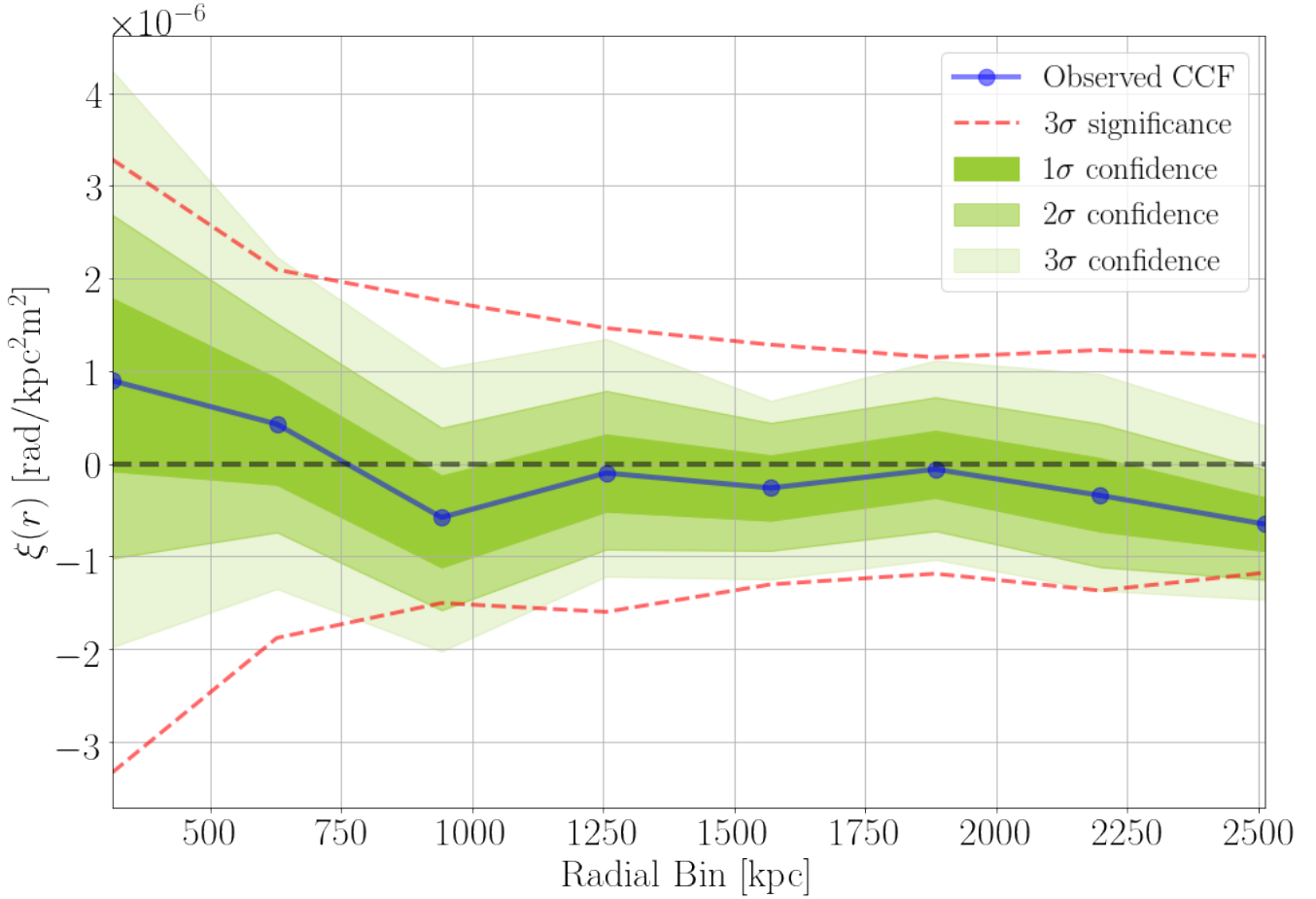


**Figure 4.** The cross-correlation function (CCF) between the  $|RRM|$ s of 1742 background sources from [Hammond et al. \(2012\)](#) and 18 million foreground galaxies selected from [Bilicki et al. \(2016\)](#). The observed CCF is shown as the solid blue line. The red dashed lines mark the  $3\sigma$  significant level of the cross-correlation, while the green coloured regions mark the confidence intervals of the cross-correlation.

#### 4.1 Predicted RM model

To place an upper bound on the magnetic field in the WHIM from our cross-correlation, we first model the rotation measure generated by the WHIM within the foreground galaxy density field,  $RM_{fil}$ . We adopt a model for  $RM_{fil}$  that is derived from the RM definition (equation 2):

$$RM_{fil,i} = 812 \sum_j \frac{1}{(1 + \bar{z}_j)^2} n_{e,fil}(z_j) B_{\parallel,fil}(z_j) \frac{1}{\sqrt{N_R(z_j)}} \Delta l_{fil}(z_j), \quad (6)$$

where  $RM_{fil,i}$  is the observed RM induced by foreground filaments over line-of-sight,  $i$ . We now explain the components of this model.

The line-of-sight integral in the RM equation is represented by a summation  $\sum_j$  over each redshift bin  $j$ . Therefore, the differential path length  $dl(z_j)$  is approximated by  $\Delta l(z_j) = l(z_{j+1}) - l(z_j)$ , where  $l(z_j)$  is the co-moving distance to redshift bin  $z_j$ :

$$l(z_j) = \frac{c}{H_0(1 + \bar{z}_j) \sqrt{\Omega_M(1 + \bar{z}_j)^3 + \Omega_\Lambda + (1 - \Omega_M - \Omega_\Lambda)(1 + \bar{z}_j)^2}}. \quad (7)$$

The foreground galaxy densities trace filaments, although filaments do not occupy the entire line-of-sight. To account for this we introduce a line-of-sight volume filling factor for filaments,  $f$ , which can range between 0 and 1, and is not a function of  $z$ . The line-of-sight path length passing through filaments is then  $\Delta l_{fil}(z_j) = f \Delta l(z_j)$ .

We include magnetic field reversals in our model, where the magnetic field changes direction over a coherence scale,  $L_c$ . We model field reversals as a random walk process ([Cho & Ryu 2009](#)). This has the effect of reducing the observed RM by  $1/\sqrt{N_R}$ , where  $N_R$  is the number of field reversals over the line-of-sight. Assuming that  $L_c < f \Delta l(z_j)$ , where  $f \Delta l(z_j)$  is the total line-of-sight covered by filaments within redshift bin  $z_j$ , the total number of field reversals along the line-of-sight passing through filaments in redshift bin  $z_j$  is then:

$$N_R(z_j) = \frac{f \Delta l(z_j)}{L_c}. \quad (8)$$

The  $RM_{fil}$  of the sources will be affected by the number of free electrons contained in filaments along the line-of-sight,

$n_{e,fil}(z_j)$ . We assume that the free electron density scales with the relative number density of galaxies:

$$n_{e,fil}(z_j) = \overline{n_{e,fil}} \left( \frac{n_{gal,2.5,i}(z_j)}{\langle n_{gal,2.5}(z_j) \rangle} \right), \quad (9)$$

where  $\overline{n_{e,fil}}$  is the average number of free electrons in filaments. The weighted galaxy count within an impact parameter of 2.5 Mpc of line-of-sight  $i$  and redshift bin  $z_j$  is given by  $n_{gal,2.5,i}(z_j) = \sum_k N_{gal,i}(r_k, z_j) \times w(r_k)$ , where  $N_{gal,i}(r_k, z_j)$  is the number of galaxies within radial impact parameter bin  $r_k$  and redshift bin  $z_j$ , and  $w(r_k)$  is the radial weighing function evaluated at radial bin  $r_k$ .  $\langle n_{gal,2.5}(z_j) \rangle$  is the average weighted galaxy count within an impact parameter of 2.5 Mpc in redshift bin  $z_j$  for all  $i$  sight-lines. Therefore, the quotient of these weighted galaxy count quantities represent whether line-of-sight  $i$  is in an under- or over-dense region.

We use the radial weighting of a King (1972) profile, given by:

$w(r) = \left(1 + \frac{r^2}{r_c^2}\right)^{-\frac{\beta}{2}}$ , where  $\beta = 0.7$  (Kronberg 2016), and we choose a scaling length of  $r_c = 1$  Mpc to correspond to the characteristic scale of filament widths (Ratcliffe et al. 1996; Doroshkevich et al. 2004; Wilcots 2004). Including a weight function allows for galaxies closer to the line-of-sight to contribute more to the  $RM_{fil}$  along that sight-line than galaxies that are farther away. This is a reasonable assumption as the magnetic field and  $n_e$ , and hence the resulting RM, will decrease as  $r$  decreases away from regions of high density.

We assume a simple magnetic field case, in which a large-scale coherent magnetic field,  $B_{fil}$ , is already in place at redshifts  $z > 0.5$ , and at  $0.1 < z < 0.5$  the field is frozen into the plasma. Thus the magnitude of the magnetic field of the IGM will scale with  $n_e$  (electron number densities) present in the foreground galaxy density. We do not consider magnetic energy injected on large-scales by compact astrophysical sources (such as AGN). This is a reasonable assumption as AGN activity becomes less common in the  $z < 2$  universe (Madau & Dickinson 2014). As such, this model is independent of magneto-genesis mechanisms.

We assume that the filaments are randomly distributed and cylindrical in shape (in the  $h \gg R$  regime, where  $h$  = height, and  $R$  = radius of a cylindrical filament). As in Blasi et al. (1999), we assume that the magnetic fields and filaments obey both flux conservation and mass conservation, to derive:

$$B_{\parallel,fil}(z_j) = B_{0,\parallel,fil} \left( \frac{n_{gal,2.5,i}(z_j)}{\langle n_{gal,2.5}(z_j) \rangle} \right)^{1/2}, \quad (10)$$

where  $B_{0,\parallel,fil}$  is the co-moving mean magnetic field strength in filaments. We assume that for scales  $< 2.5$  Mpc, IGM filaments are gravitationally bound structures, and thus equations 9 and 10 contain no direct cosmological dependence.

Including the above assumptions, equation 6, the model for the predicted RM due to filaments in a foreground galaxy density grid becomes:

$$RM_{fil,i} = 812 \sum_j \frac{f^{1/2}}{(1+z_j)^2} \overline{n_{e,fil}} B_{\parallel,fil,0} \times \left( \frac{n_{gal,2.5,i}(z_j)}{\langle n_{gal,2.5}(z_j) \rangle} \right)^{3/2} \sqrt{\frac{L_c}{\Delta l(z_j)}} \Delta l(z_j). \quad (11)$$

## 4.2 Upper Bounds

### 4.2.1 Generating Upper Bounds

We can use equation 11 to calculate the predicted  $RM_{fil}$  along the sight-lines of the 1742 observed RM sources used in this study. As in Section 3.3 using equation 5, we can calculate the cross-correlation between the 1742 predicted  $RM_{fils}$  and the foreground galaxy densities. Since  $B_{\parallel,fil,0}$  is an input to equation 11, we determine the  $B_{\parallel,fil,0}$  required to scale the resulting cross-correlation above the  $3\sigma$  significance levels (as calculated in Section 3.4.2).

The cross-correlation is measured at 8 linearly spaced radial bins extending to 2.5 Mpc. Therefore we chose to scale the resulting predicted cross-correlation to  $3\sigma$  at the radial bin closest in value to the input coherence scale ( $L_c$ ) of the magnetic field. The input  $B_{\parallel,fil,0}$  to produce  $RM_{fils}$  that correlate above  $3\sigma$  in the radial bin closest in value to  $L_c$  is the upper bound on the IGMF. We then can determine the average RM induced by the IGMF of foreground filaments,  $\langle RM_{fil} \rangle$ , by taking the ensemble average of each individual  $RM_{fil}$  over all 1742 sight-lines.

In order to do this calculation, we must assume values for the mean electron number density in filaments ( $\overline{n_{e,fil}}$ ), the coherence scale of the IGMF ( $L_c$ ), and filling factor ( $f$ ). Alternatively, from the model RM we derived in equation 11, we can place bounds on the combination of these parameters  $f^{1/2} \overline{n_{e,fil}} B_{\parallel,fil,0}$ .

Because the origin of these fields are unknown and no previous direct observations exist, we chose to test a set of 5 coherence scales: 0.5, 1.0, 1.5, 2.0, and 2.5 Mpc. We cannot probe scales larger than 2.5 Mpc as our correlation scale does not extend further than its largest radial bin. We find that the upper bound on  $f^{1/2} \overline{n_{e,fil}} B_{\parallel,fil,0}$  is similar for all scales tested, all on the order of  $\sim 10^{-8} \mu\text{G cm}^{-3}$ . For the largest coherence scale of 2.5 Mpc, we obtain an upper bound of  $f^{1/2} \overline{n_{e,fil}} B_{\parallel,fil,0} < 7.6 \times 10^{-8} \mu\text{G cm}^{-3}$ , corresponding to an average RM enhancement of 4.7 rad/m<sup>2</sup> due to filaments in the observer frame. The upper bounds for the other coherence scales are found in column 2 of Table 1, these upper bounds are plotted in Figure 6 as a function of coherence scales for a visual representation.

To further constrain  $B_{\parallel,fil,0}$ , we make assumptions about  $f$  and  $\overline{n_{e,fil}}$ . The filling factor of filaments within the IGM is not well constrained. Simulations have shown that  $f = 0.06$  at lower redshifts ( $z < 0.5$ ) (Aragón-Calvo et al. 2010; Cautun et al. 2014; Davé et al. 2010). The average free electron density within filaments is also not well constrained because filaments are difficult to directly observe (Cantalupo et al. 2014); most values on the average electron densities come from simulations. These studies quote values from  $10^{-4}$  to  $10^{-6} \text{cm}^{-3}$  (Cen & Ostriker 2006; Ryu et al. 2008; Akahori & Ryu 2010), as in O'Sullivan et al. (2019) here we adopt a typical value  $\overline{n_{e,fil}} \approx 10^{-5} \text{cm}^{-3}$ .

The upper bounds of  $B_{\parallel,fil,0}$  for the various coherence scales are found in column 3 of Table 1. For the largest scale we test, and the above values used for  $\overline{n_{e,fil}}$  and  $f$  we obtain a  $3\sigma$  upper bound on the IGMF to be 31 nG for a coherence scale of 2.5 Mpc. We find little difference between the IGMF upper bound between 1.0 to 2.5 Mpc. We found that the  $3\sigma$  upper bound on the IGMF for the smallest coherence scale of 0.5 Mpc is 44 nG. This value is much less constraining due to the fact that the error bars at this scale are larger, and therefore not ideal to use as an upper bound compared to the other scales.

The associated predicted  $RM_{fils}$  generated using equation 11 can be seen in the left panel of Figure 5, in which we also compare



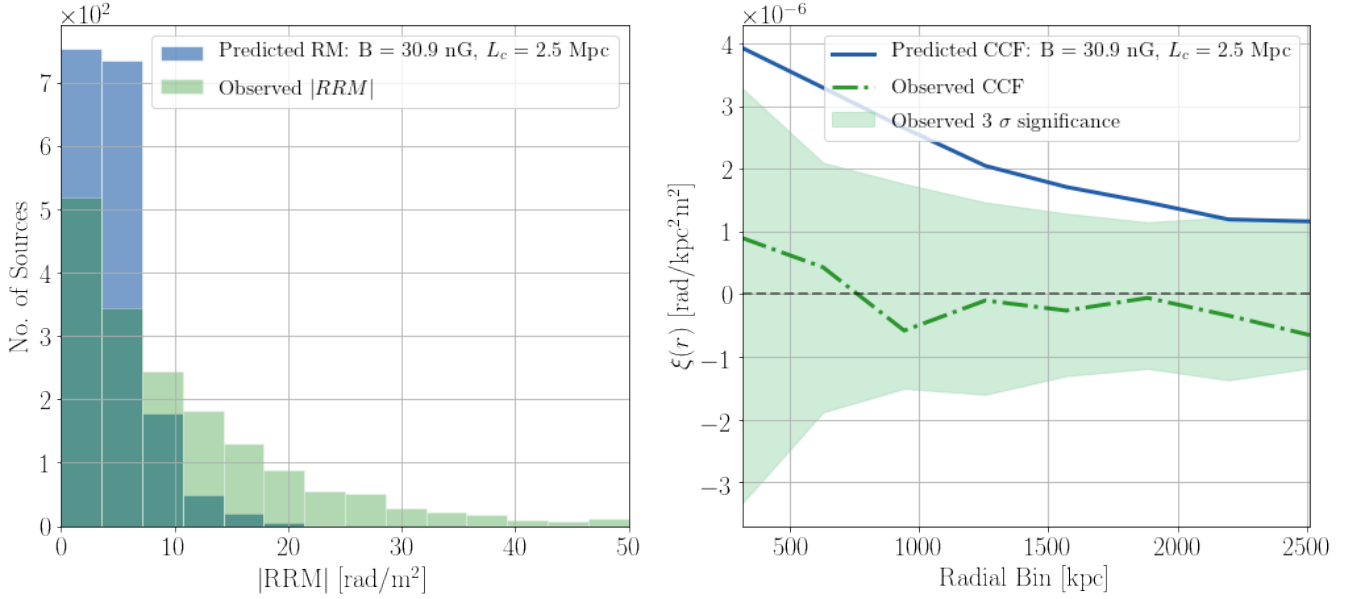


**Figure 5.** **Left:** Distribution of predicted RM values compared to observed  $|RRM|$  values used, generated using the model given in equation 11, using  $\bar{n}_{e,fil} = 10^{-5} \text{ cm}^{-3}$ ,  $f = 0.06$ , and  $L_c = 2500 \text{ kpc}$ . **Right:** The resulting cross-correlation function from the observed and predicted RMs shown in the left panel. The green shaded region corresponds to the red dashed lines indicating a  $3\sigma$  significance level in Figure 4.

Coherence Scale ( $L_c$ )	$f^{1/2} \bar{n}_{e,fil} B_{\parallel,fil,0}$ Upper Bound	$B_{\parallel,fil,0}$ Upper Bound	$\langle RM_{fil} \rangle$ Upper Bound
0.5 Mpc	$1.1 \times 10^{-7} \mu\text{G cm}^{-3}$	44 nG	$3.0 \pm 1.9 \text{ rad/m}^2$
1.0 Mpc	$7.9 \times 10^{-8} \mu\text{G cm}^{-3}$	32 nG	$3.1 \pm 2.0 \text{ rad/m}^2$
1.5 Mpc	$7.3 \times 10^{-8} \mu\text{G cm}^{-3}$	30 nG	$3.5 \pm 2.3 \text{ rad/m}^2$
2.0 Mpc	$6.6 \times 10^{-8} \mu\text{G cm}^{-3}$	27 nG	$3.7 \pm 2.4 \text{ rad/m}^2$
2.5 Mpc	$7.6 \times 10^{-8} \mu\text{G cm}^{-3}$	31 nG	$4.7 \pm 3.0 \text{ rad/m}^2$

**Table 1.** Table containing the results for constraints on the magnetic field within filaments, using the predicted RM model (equation 11) as derived in section 4.1 for various tested coherence scales,  $L_c$ . Column 1: The coherence scales tested; Col. 2:  $3\sigma$  upper bound on the combined quantity  $f^{1/2} \bar{n}_{e,fil} B_{\parallel,fil,0}$ , for the associated coherence scale; Col. 3:  $3\sigma$  upper bounds on  $B_{\parallel,fil,0}$  assuming  $f = 0.06$  and  $\bar{n}_{e,fil} = 10^{-5} \text{ cm}^{-3}$  for the associated coherence scales; Col. 4: The average upper bound RM induced by filaments in foreground large-scale structure, calculated by taking the average of each individual  $RM_{fil,i}$ . The uncertainty on this quantity is given by calculating the  $1\sigma$  standard deviation.

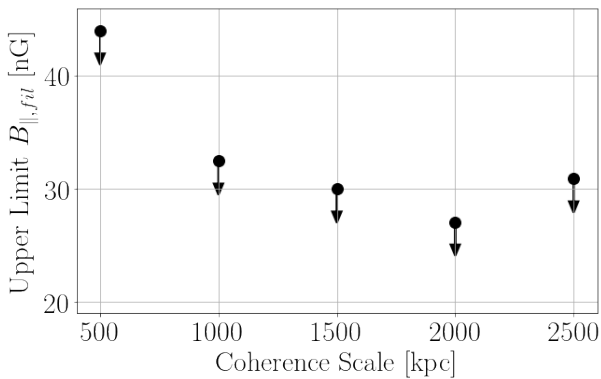


**Figure 6.** Upper bounds on the IGMF for all coherence scales tested in this study, the exact values can be found in Table 1.

to the observed RRM values used to calculate the cross-correlation in Section 3.3. The right panel of Figure 5 shows the resulting cross-

correlation function calculated using the predicted  $RM_{fils}$ , this output correlation is greater than  $3\sigma$  at the largest radial bin - allowing us to use the associated  $B_{\parallel,fil,0}$  value as an upper bound.

#### 4.2.2 Effects of Model Assumptions on Upper Bounds

To ensure that the choice of weighting functions and parameters produced robust upper limits, we tested scaling length values,  $r_c$ , between 0.5 Mpc and 2.5 Mpc, and found that the final upper bound  $B_{\parallel,fil,0}$  results were consistent within  $\pm 10\%$  for  $L_c = 1 - 2.5 \text{ Mpc}$ , and within  $\pm 30\%$  for  $L_c = 0.5 \text{ Mpc}$ , for all  $r_c$  values tested. We also found that the choice of a King (1972) profile matched the upper bounds results from using a Gaussian profile, within  $\pm 15\%$ . Therefore we conclude that the choice of weighting function and scaling lengths are not a source of major uncertainty in our methods.

We assumed a cylindrical symmetry for filaments, along with mass and flux conservation, to derive equation 10. Blasi et al. (1999) used the same assumptions as our study, although invoked

spherical symmetry, to derive  $B \sim n_e^{2/3}$  (a relation used in IGMF studies such as Pshirkov et al. 2016; O’Sullivan et al. 2020). When using the  $B \sim n_e^{2/3}$  scaling relation in our study, we obtain upper bound results that are  $\sim 15\%$  lower than those quoted in Table 1. The scaling relation  $B \sim n_e^k$  of magnetic fields with various gas densities has been previously explored in the literature (see Vallée 1995 for a thorough review). Using measurements from previous studies, Vallée (1995) concludes that for low gas densities  $n_e < 100 \text{ cm}^{-3}$ ,  $k = 0.17 \pm 0.03$ . When using this scaling relation in our model, we find that the upper bound results increase by  $\sim 40\%$ . While the exponent of the magnetic field and density scaling does have an implication on our results, it is not significant. The upper bounds on the combined factor  $f^{1/2} \overline{n_{e,fil}} B_{\parallel,fil,0}$  are more robust than those for  $B_{\parallel,fil,0}$  because we include further assumptions of values of  $\overline{n_{e,fil}}$  and  $f$ . We tested various filling factors to understand the effect on our resulting upper bounds. In our calculations, we assumed  $f = 0.06$ . For a lower value  $f = 0.01$ , and for a higher value  $f = 0.2$ , we find an increase by  $\sim 145\%$  and a decrease by  $\sim 45\%$  in the upper bound on all scales, respectively.

As discussed in Section 4.2, simulations have shown that  $\overline{n_{e,fil}}$  can vary between  $10^{-4} \text{ cm}^{-3}$  and  $10^{-6} \text{ cm}^{-3}$ . In our quoted upper bounds, we assumed  $10^{-5} \text{ cm}^{-3}$ . Changing  $\overline{n_{e,fil}}$  in equation 9 to test the extreme range for filaments, we find that the resulting upper bounds increase and decrease by an order-of-magnitude for  $\overline{n_{e,fil}} = 10^{-6} \text{ cm}^{-3}$  and  $\overline{n_{e,fil}} = 10^{-4} \text{ cm}^{-3}$ , respectively, for all  $L_c$  values. While the changes in both  $f$  and  $n_e$  cause a more drastic change in the upper bound values we obtain, these are also the least well-constrained values used within our study.

### 4.3 Comparison To Other Studies

It is difficult to make direct comparisons between upper bound studies, as the techniques and data used differ greatly. Also, knowledge of many of the values we assume ( $n_e, L_c$ , and  $f$ ) in our study are not robustly known, and thus values assumed vary between studies. Techniques to place bounds come from statistical methods, observations, and simulations. Furthermore, because of the lack of observations, simulations have been used to place bounds on the IGMF. These range from simulated observables for forecasting future radio polarimetric surveys, to full universe magneto-hydrodynamic (MHD) simulations.

Vazza et al. (2017) used the MHD ENZO (Bryan et al. 2014) code and incorporated galaxy formation, dark matter, gas, and chemical abundances, to simulate cosmic magnetic field evolution from  $z = 38$  to  $z = 0$ . Whereas most cosmic simulations focus on a single magneto-genesis model, Vazza et al. (2017) incorporate both primordial and astrophysical seeding models to compare output observables (such as Faraday rotation, synchrotron emission, cosmic ray propagation, etc.). They found that the magnetic fields in higher density regions such as within galaxy clusters and groups were on the order of  $\mu\text{G}$  for all scenarios, whereas in the less dense filament environments, the magnetic field strength strongly depends on the magneto-genesis models assumed. For purely astrophysical phenomena, they found filaments to be magnetized at the nG level, whereas for purely primordial fields magnetic fields are found to be  $\sim 0.1 \text{ nG}$ , and for dynamo amplification models they find fields on the order of  $100 \text{ nG}$ . Our upper-bound values possibly disfavoured the dynamo amplification models from Vazza et al. (2017), for which the simulations start with a weak seed field of  $10^{-9} \text{ nG}$  and allow for dynamo amplification of these

fields through solenoidal turbulence within large scale structure. However, in general the magnetic field bounds we have placed in this study are not stringent enough to be able to discern between pure primordial vs. pure astrophysical models.

In Table 2, we list upper bounds on the IGMF from relevant observational studies. We will discuss a subset of them in further detail below.

Observationally, upper bounds placed on the IGMF are extremely limited - this is mostly due to the estimated low electron densities in filaments (Cen & Ostriker 2006). Notably, observing a giant double-lobed radio galaxy, O’Sullivan et al. (2019) determined that one of the galaxy’s radio lobes passed through an IGM filament, allowing them to single out the RM due to the filament. This RM corresponded to a density weighted upper bound of  $\sim 0.3 \mu\text{G}$ . This is consistent with, but less constraining than, the upper limit we have derived here.

Xu et al. (2006) provided IGMF upper bounds from a large statistical study using RM data derived from Simard-Normandin & Kronberg (1980) (with and without redshift information), and LSS information from galaxy counts in the Hercules and Perseus-Pisces superclusters (from the second Center for Astrophysics survey, CfA2, and the Two Micron All Sky Survey, 2MASS, galaxy catalogues). They used RMs smoothed at a scale of  $7^\circ$  (smoothed RMs, SRM) to study very large scale variations. Xu et al. (2006) then looked for averaged correlations across known super-cluster structures between the averaged SRMs within the region, and the galaxy-count-weighted path-length through the structure. They use a very simple model for RMs induced from a filament, with similar but less complex components compared to our model, such as; coherence scale ( $L_c$ ), free electrons in filaments ( $\overline{n_{e,fil}}$ ), path length through filament structures, and  $B_{\parallel,fil,0}$ .

Xu et al. (2006) obtained upper bounds by comparing expectations between this simple RM model and the SRMs in the Hercules cluster. Testing values of  $L_c = 200 \text{ kpc} - 800 \text{ kpc}$  and  $n_{e,fil,0} = 0.5 - 2 \times 10^{-5} \text{ cm}^{-3}$ , they obtain upper bounds between  $0.4$  and  $0.3 \mu\text{G}$ . These bounds are larger than ours for a multitude of reasons such as: fewer RM sources and galaxies used, and not subtracting off the GRM. This sort of correlation and analysis was done looking at averaged and smoothed values over the entire structure, while our approach calculates a cross-correlation function across all RM sight-lines.

Various other statistical methods have been used to place bounds, each with their own respective strengths and weaknesses. A large source of error with these types of analyses is accurately subtracting the Galactic foreground contribution from RMs so that we only obtain extragalactic signals (see equation 3). If sources occupy the same region of sky, the Galactic component of the RM is comparable between the sources. Vernstrom et al. (2019) used this to determine limits for the IGMF by comparing statistical RM differences between populations of physical pairs of extragalactic polarized sources (found at similar redshifts and close on the sky) versus populations of non-physical pairs (occupying different redshifts but still close together on the plane of the sky) within the Hammond et al. (2012) RM catalogue. The statistical differences between the RMs of these populations would be due to the extra rotation induced on the non-physical pairs from the IGMF, allowing upper limits of  $40 \text{ nG}$  to be placed on the parallel component of  $B_{IGM}$ . This value broadly agrees with our bounds at  $24 \text{ nG}$ , using a subset of the same RM catalogue though using different techniques.

Following the same novel technique as Vernstrom et al. (2019), O’Sullivan et al. (2020) used RMs of 201 physical and 148 ran-

**Table 2.** A selection of relevant observational upper bounds on large scale extragalactic magnetic fields within the filamentary IGM, sorted by increasing IGMF upper bound.

Upper Bound	Coherence Scale ( $L_c$ )	Redshift Range	Reference	Technique Summary
0.65 nG 1.7 nG	Jean's scale ( $\lambda_j(z)$ ) $1/H_0$	$0 < z < 5$	Pshirkov et al. (2016)	RM vs. $z$
1 nG 6 nG	$1/H_0$ 50 Mpc	$0 < z < 2.5$	Blasi et al. (1999)	RM vs. $z$
4 nG	$L_c/\lambda_j(z=0) \leq 1000$	Unknown <sup>5</sup>	O'Sullivan et al. (2020)	$\Delta$ RM between adjacent sources
21 nG	$\sim \text{Gpc}^6$	$z \sim 0.1$	Ravi et al. (2016)	RRM from FRB 150807
27 nG - 44 nG	2.5 Mpc - 0.5 Mpc	$0.1 < z < 0.5$	This paper	RRM cross-correlation
30 nG	$\theta = 1^\circ$ <sup>7</sup>	$z < 0.048$	Brown et al. (2017)	Synchrotron cross-correlation
30 nG - 60 nG	2 Mpc	$\langle z \rangle = 0.14 \pm 0.01$	Vernstrom et al. (2021)	Statistically Stacking Filaments
30 nG - 1980 nG	1 - 4 Mpc	$0 < z < 0.57$	Vernstrom et al. (2017)	Synchrotron cross-correlation
37 nG	1 Mpc	$0 < z < 1$	Vernstrom et al. (2019)	$\Delta$ RM between adjacent sources
250 nG	$\sim 10$ Mpc	$0.095 < z < 0.142$	Locatelli et al. (2021)	Non-detection of filament accretion shocks
300 nG	300 kpc	$z \sim 0.34$	O'Sullivan et al. (2019)	Observed intervening filament
300 nG	0.5 Mpc	$0.0304 < z < 0.0414$ <sup>8</sup>	Xu et al. (2006)	RM correlation with galaxy counts

<sup>5</sup> Redshift information not used

<sup>6</sup> Averaged over full sight-line

<sup>7</sup> Cross-correlation computed on an angular scale

<sup>8</sup> The redshift range of the Hercules super-cluster was determined by Kopylova & Kopylov (2013)

dom pairs derived from the LOFAR Two-Metre Sky Survey (LoTSS) DR1 (Shimwell et al. 2019). They found an upper bounds on the magnetic field of the IGM of 4nG at Mpc scales. Because LoTSS is observed at 144 MHz, any RMs derived from these bands are extremely sensitive to any Faraday depolarization, therefore the authors conclude that these sources preferentially occupy less dense and weakly magnetized regions within the IGM - such as on the boundaries of filaments and voids. In contrast, the 1.4 GHz sample used in both Vernstrom et al. (2019) and our study are less susceptible to Faraday depolarization and the bounds on the IGM derived from these data should be more representative of denser filaments. Because the bounds we derived use the same 1.4 GHz RM data (Hammond et al. 2012) and obtain similar magnetic field upper limit as Vernstrom et al. (2019), we cannot disfavour the hypothesis that LoTSS sources occupy rarefied environments.

The hypothesis that LoTSS sources occupy extremely rarefied environments was further confirmed by Stuardi et al. (2020), who looked at 37 polarized LoTSS giant radio galaxies (GRGs) - galaxies whose outer lobes extend well into the IGM and have a limiting size of 700 kpc. Using the same approaches as Vernstrom et al. (2019) and O'Sullivan et al. (2020), they analyzed the RM differences between the lobes of each of the galaxies. They found that the RM difference between the lobes of the galaxies were consistent with variations in the local Milky Way Galactic foreground magnetic field, as was found by Vernstrom et al. (2019). Stuardi et al. (2020) also found that there were small amounts of Faraday depolarization between 144 MHz and 1.4GHz,  $D_{144\text{MHz}}^{1.4\text{GHz}} > 0.03$  for all sources. This can be explained by the presence of a low density medium ( $n_e \sim 10^{-5}\text{cm}^{-3}$ ) with magnetic fields on the order of 0.1  $\mu\text{G}$ , tangled on kpc scales. While it is unclear whether these sources probe the same IGM component as our studies, this

study showed the capabilities of using GRGs to study intergalactic magnetic fields as more data becomes available.

On scales smaller than we probe here, Lan & Prochaska (2020) used similar cross-correlation and analysis techniques to ours, between 1100 background RRM ( $z > 1$ , using redshift information from Hammond et al. 2012, RM information from Farnes et al. 2014, and foreground GRM subtraction from Oppermann et al. 2015) and foreground galaxy distributions as sampled by the DESI Legacy Imaging Surveys (Dey et al. 2019), to extract the characteristic RM and  $\langle B_{\parallel} \rangle$  of the circum-galactic medium (CGM) around galaxies. They obtained a null correlation, but used the trend between  $\sigma_{RM}$  and  $N_{gal}$  (number of foreground galaxies within the RRM line-of-sight) to model the random field reversals due to intersecting magnetic fields of the CGM. They use the  $3\sigma$  significance levels on  $\sigma_{RRM}$  vs.  $N_{gal}$  and a random walk model to place upper bounds. They found  $3\sigma$  upper bounds of  $RM_{CGM} \sim 15 \text{ rad m}^{-2}$  and  $B_{\parallel,CGM} < 2\mu\text{G}$  within the CGM virial radius (impact parameters less than 200 kpc).

Using a combination of the cross-correlation methods from Lan & Prochaska (2020) and our study, with foreground galaxy density maps and denser RM grids, we can hope to accurately probe the magnetic fields of the CGM, and the transition region between the CGM and the IGM (the CGM is thought to extend between 100 kpc - 200 kpc from individual galaxies, Shull 2014). The finer precision of denser RM grids will allow to accurately measure correlations at these scales (Bernet et al. 2010, 2013; Farnes et al. 2014; Prochaska & Zheng 2019). Understanding the magnetic properties of this transition region is key to understanding the interplay between the properties of the IGM, CGM, and galaxies themselves (Borthakur et al. 2015). Additionally, this region mediates the acquiring of neutral gas from the IGM to individual

galaxies to further fuel star formation and other galactic processes. Furthermore, exploring the gas and metal properties of the CGM and IGM may allow us to differentiate between various galaxy formation models (Tumlinson et al. 2017; Codoreanu et al. 2018). Cross-correlation techniques can also be used to detect the synchrotron cosmic web (which is also much too faint to directly observe), and hence constrain the perpendicular component of the IGMF in filaments. This was recently done by Brown et al. (2017) by cross-correlating S-PASS continuum data at 2.3 GHz and MHD simulations of the cosmic web (using models by Dolag et al. 2005; Donnert et al. 2009), placing bounds on the order of  $0.1 \mu\text{G}$  on the IGMF. The upper bound places by Brown et al. (2017) agreed with other synchrotron based bounds placed, such as in Vernstrom et al. (2017), and is consistent with bounds placed in our study.

Most recently Locatelli et al. (2021) used the non-detection of synchrotron accretion shocks between two adjacent galaxy clusters located using LOFAR (pair 1: RXCJ1155.3+2324 /RXCJ1156.9+2415, and pair 2: RXCJ1659.7+3236/RXCJ1702.7+3403) by comparing their observations to MHD ENZO (Bryan et al. 2014) simulations of galaxy clusters of similar properties. By doing this they were able to place bounds on the intergalactic magnetic field present to  $B_{fil} < 0.25 \mu\text{G}$  for Mpc scales. Although these bounds are consistent but less constraining than those places in our study, Locatelli et al. (2021) used only two clusters. With more cluster observations with radio telescopes such as LOFAR this technique can prove to be powerful.

Forecasts of future radio surveys have lead to predictions for what such an IGMF signal would look like, if detected. Staszczyn et al. (2010) found, using cross-correlations of simulated data (a similar technique to our study), that direct detections of the large-scale magnetic field that permeates the IGM in filaments will only be possible with larger RM catalogues from future telescopes. Akahori et al. (2014) explored the effectiveness of using simulated RM grids with varying sample sizes and statistical techniques to detect magnetic fields structure in filaments. They found that basic properties of large-scale magnetic fields can be determined statistically using upcoming surveys, allowing us to distinguish between magneto-genesis models. For our study, it is not possible to analyze the shape of our cross-correlation function to obtain information about the coherence scale of the IGMF, nor to constrain the generation mechanism of the field, as we did not detect a significant cross-correlation signal. Such studies must wait for future surveys.

#### 4.4 Sources of Uncertainty

Our study is mostly limited by the availability of extra-galactic RM sources with redshift information. As we progress towards an era of large data availability, such as the upcoming data releases from the Australian Square Kilometre Array Pathfinder (ASKAP) within the next few years, the bounds we can place on  $B_{\parallel,fil}$  will become more robust. Once completed, ASKAP's Polarization Sky Survey of the Universe's Magnetism (POSSUM)<sup>9</sup> (Gaensler et al. 2010) will comprise the largest catalogue of extra-galactic rotation measures to date, with RMs for one million extra-galactic radio sources with a source-density coverage of  $\geq 25$  RMs  $\text{deg}^{-2}$ . To demonstrate that using this technique with a larger sample of

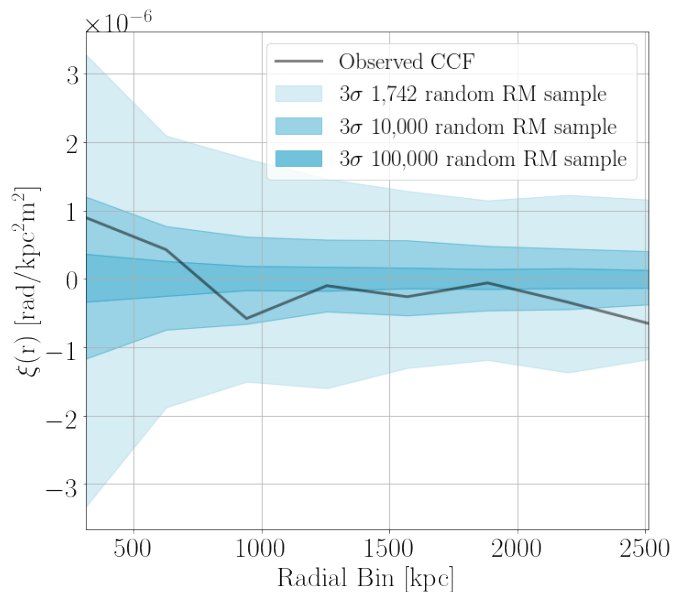


**Figure 7.** The  $3\sigma$  significance levels of random CCFs for increasing sample sizes of RRM sources. The RRRMs were generated by generating randomized sightlines and using RRRMs from real data.

RRMs will obtain more stringent upper bounds, we generated simulated RM data using the technique described in Section 3.4.2 to obtain sample catalogues of 1742 RMs (the size of the Hammond et al. 2012 sample used in this study, for comparison), 10,000 RMs, and 100,000 RMs. We then obtain  $3\sigma$  significance levels for 1000 realizations of sample catalogues of these sizes, plotted in Figure 7. For the sample sizes larger than 1742, we draw RM values (with replacement) from the full Taylor et al. (2009) catalogue, applying the same sample cuts as in section 3.1, and analysis in section 3.2 to obtain RRRMs. The error bars become smaller with increasing sample sizes. At the largest radial bin, 2.5 Mpc, this corresponds to a  $\sim 3$  times better sensitivity for a sample size of 10,000 RMs than for a sample size of 1742 RMs, whereas a sample size of 100,000 RMs correspond to  $\sim 9$  times better sensitivity at scales of 2.5 Mpc. With the data to become available from surveys such as POSSUM, we expect that this method will far better constrain  $B_{\parallel,fil}$ .

The main source of uncertainties in this analysis originates from the data-sets used. Hammond et al. (2012) use RMs determined from NVSS, which is determined by linearly fitting the polarization angle vs.  $\lambda^2$  for only 2 narrowly spaced bands (see Section 2.1), which may lead to spurious RM values for sources.

These spurious RMs could manifest in  $n\pi$  ambiguities. In this case the phase angles wrap around at  $\pi$  and thus the observed polarization angle is only known to modulo  $n\pi$  radians (Heald 2009). Sources affected by this could have erroneously high RMs offset from the true RM by  $\pm 652.9 \text{ rad/m}^2$  (Ma et al. 2019a). Ma et al. (2019a) explored this effect in the Taylor et al. (2009) catalogue by using follow up large-bandwidth observations of suspicious sources. They concluded that the  $n\pi$  ambiguity would affect  $> 50$  sources in the full  $\sim 37,000$  sample catalogue.

Additionally, the Taylor et al. (2009) catalogue does not adequately treat Faraday thick sources. Faraday thick sources are polarized sources whose fractional polarization varies from the linear relationship with  $\lambda^2$  assumed by Taylor et al. (2009). This Faraday thick behaviour can be caused by many situations; regions

<sup>9</sup> <http://askap.org/possum>

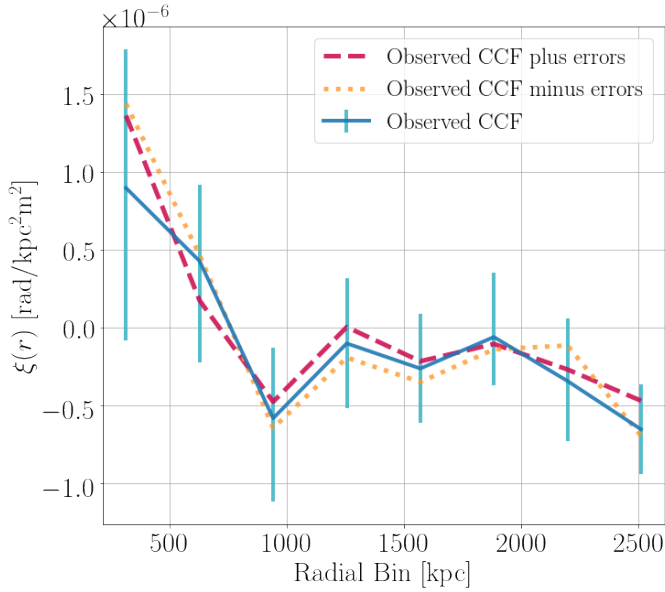


**Figure 8.** The resulting cross-correlation functions when we include the errors associated with the RM sources. The red dashed line is calculated by adding a random Gaussian drawn fraction of the error to the  $|RRM|$  value, while the orange line is calculated in the same manner but the errors are subtracted from the  $|RRM|$  values.

simultaneously emitting and rotation, or various regions rotating at different amounts along the line-of-sight (see a detailed discussion in Sokoloff et al. 1998). Because the two bands used to produce the RMs of these sources are spaced close together, the RM information captured could be from a particular Faraday rotating structure and not representative over larger bandwidths. However, for both of these cases without re-observing all sources at larger bandwidths, it is impossible to determine which sources would be affected. POSSUM will observe at 800 MHz to 1088 MHz at 1 MHz resolution, corresponding to  $\Delta\nu = 288$  MHz, leading to much more robust RM value assignments. Additionally, POSSUM will use techniques such as QU-fitting (O’Sullivan et al. 2012) and RM synthesis (Brentjens & de Bruyn 2005) to extract Faraday depth information and RMs from sources. These techniques are much more reliable than angle fitting techniques used for older data-sets.

We did not use the error bars associated with the Hammond et al. (2012) RM sources in our cross-correlation. To ensure that the RM errors would not have an effect on the resulting cross-correlation function, we recalculated the cross-correlation for values of RM adjusted by a Gaussian drawn value multiplied by its error. We found that running this for 100 cases did not change the outcome of the cross-correlation function within  $1\sigma$ . This effect can be seen for one run in Figure 8.

## 5 CONCLUSION

Because of the low gas densities in cosmic web filaments, cosmic magnetic fields are difficult to detect, with estimated values in the nG regime. These weak magnetic fields require statistical approaches to extract their signal from large data-sets.

We use a cross-correlation statistical approach between 1742 background RMs (from Hammond et al. 2012,  $z > 0.5$ ) and the superCOSMOSxWISE all-sky photometric redshift catalogue

of 18 million galaxy sources (Bilicki et al. 2016) to trace large scale structure between  $0.1 < z < 0.5$ ). We used the Oppermann et al. (2015) Galactic rotation measure (RM) map to determine the residual rotation measures (RRMs). We then perform a cross-correlation between the background RRM and the foreground galaxy density maps over 3 redshift bins ( $0.1 < z < 0.2$ ,  $0.2 < z < 0.3$ , and  $0.3 < z < 0.5$ ) at impact parameters between  $\sim 0.5$  Mpc to 2.5 Mpc.

Our results are as follows:

- (i) We found no statistically significant correlation between RRM and the foreground galaxy density.
- (ii) We used a simple model and the  $3\sigma$  significance levels from the observed cross-correlation to place an upper bound on the mean co-moving magnetic fields within filaments. The  $3\sigma$  upper bound for magnetic field coherence scales between 1 - 2.5 Mpc was  $\sim 30$  nG (the magnitude was similar for all 4 scales probed), and 44 nG for 0.5 Mpc. These upper bounds depend on assumptions for the filling factor and mean electron density.
- (iii) Comparing our result to simulations of Vazza et al. (2017) tends to disfavour dynamo amplification models of magneto-genesis, though we cannot discern between primordial and astrophysical magneto-genesis models. We found that this upper bound agreed well with upper bounds derived from other past statistical studies. A statistical study by O’Sullivan et al. (2020) using 144 MHz LoTSS RM data suggested a small upper bound of  $< 0.5$  nG, but focuses on less dense regions of the IGM and thus were placing bounds on magnetic fields in less dense media.

The main limitations with our method is the relatively small sample size of RMs, and the potentially unreliable way the RMs were determined in the NVSS-derived catalogue. Future data-sets in the ASKAP and SKA era will allow for more robust bounds to be placed on these elusive intergalactic magnetic fields.

## ACKNOWLEDGEMENTS

We thank the anonymous referee for their useful comments. We also thank Lawrence Rudnick, Franco Vazza, Dongsu Ryu, Yik Ki (Jackie) Ma, Shane O’Sullivan, Ue-Li Pen, Cameron Van Eck, Mubdi Rahman, Norm Murray, and Matthew Young for useful discussions.

This research has made use of the SIMBAD database, operated at CDS, Strasbourg, France, and the NASA/IPAC Extragalactic Database (NED), which is funded by the National Aeronautics and Space Administration and operated by the California Institute of Technology.

The Dunlap Institute is funded through an endowment established by the David Dunlap family and the University of Toronto. We acknowledge the support of the Natural Sciences and Engineering Research Council of Canada (NSERC) through grant RGPIN-2015-05948, and of the Canada Research Chairs program. This work was performed traditional land of the Huron-Wendat, the Seneca, and most recently, the Mississaugas of the Credit River.

## DATA AVAILABILITY

The Hammond et al. (2012) RM-redshift data underlying this article was accessed from <https://web.archive.org/web/20170519211023/http://www.sifa.org.au/Main/>

**RM Catalogue**, the **Oppermann et al. (2015)** Galactic RM data was accessed from <https://wwwmpa.mpa-garching.mpg.de/ift/faraday/>, and the **Bilicki et al. (2016)** galaxy catalogue was accessed from the Wide Field Astronomy Unit at the Institute for Astronomy, Edinburgh at <http://ssa.roe.ac.uk/WISExSCOS>. The derived data generated in this research will be shared on reasonable request to the corresponding author.

## REFERENCES

- Aihara H., et al., 2011, *ApJS*, **193**, 29
- Akahori T., Ryu D., 2010, *ApJ*, **723**, 476
- Akahori T., Gaensler B. M., Ryu D., 2014, *ApJ*, **790**, 123
- Akahori T., Ryu D., Gaensler B. M., 2016, *ApJ*, **824**, 105
- Aragón-Calvo M. A., van de Weygaert R., Jones B. J. T., 2010, *MNRAS*, **408**, 2163
- Bernet M. L., Miniati F., Lilly S. J., Kronberg P. P., Dessauges-Zavadsky M., 2008, *Nature*, **454**, 302
- Bernet M. L., Miniati F., Lilly S. J., 2010, *ApJ*, **711**, 380
- Bernet M. L., Miniati F., Lilly S. J., 2013, *ApJ*, **772**, L28
- Bilicki M., et al., 2016, *ApJS*, **225**, 5
- Blasi P., Burles S., Olinto A. V., 1999, *ApJ*, **514**, L79
- Bonafede Feretti, L. Murgia, M. Govoni, F. Giovannini, G. Dallacasa, D. Dolag, K. Taylor, G. B. 2010, *A&A*, **513**, A30
- Bonafede A., Vazza F., Brüggem M., Murgia M., Govoni F., Feretti L., Giovannini G., Ogrean G., 2013, *MNRAS*, **433**, 3208
- Borthakur S., et al., 2015, *ApJ*, **813**, 46
- Bregman J. N., 2007, *ARA&A*, **45**, 221
- Brentjens M. A., de Bruyn A. G., 2005, *A&A*, **441**, 1217
- Brown S. D., 2011, *Journal of Astrophysics and Astronomy*, **32**, 577
- Brown S., et al., 2017, *MNRAS*, **468**, 4246
- Bryan G. L., et al., 2014, *ApJS*, **211**, 19
- Cantalupo S., Arrigoni-Battaia F., Prochaska J. X., Hennawi J. F., Madau P., 2014, *Nature*, **506**, 63
- Cautun M., van de Weygaert R., Jones B. J. T., Frenk C. S., 2014, *MNRAS*, **441**, 2923
- Cen R., Ostriker J. P., 1999, *ApJ*, **514**, 1
- Cen R., Ostriker J. P., 2006, *ApJ*, **650**, 560
- Cheng B., Olinto A. V., Schramm D. N., Truran J. W., 1996, *Phys. Rev. D*, **54**, 4714
- Cho J., Ryu D., 2009, *ApJ*, **705**, L90
- Clarke T. E., Kronberg P. P., Böhringer H., 2001, *ApJ*, **547**, L111
- Codoreanu A., Ryan-Weber E. V., García L. Á., Crighton N. H. M., Becker G., Pettini M., Madau P., Venemans B., 2018, *MNRAS*, **481**, 4940
- Condon J. J., Cotton W. D., Greisen E. W., Yin Q. F., Perley R. A., Taylor G. B., Broderick J. J., 1998, *AJ*, **115**, 1693
- Davé R., Oppenheimer B. D., Katz N., Kollmeier J. A., Weinberg D. H., 2010, *MNRAS*, **408**, 2051
- Dey A., et al., 2019, *AJ*, **157**, 168
- Dolag K., Grasso D., Springel V., Tkachev I., 2005, *Journal of Cosmology and Astroparticle Physics*, 2005, 009
- Dolag K., Meneghetti M., Moscardini L., Rasia E., Bonaldi A., 2006, *MNRAS*, **370**, 656
- Donnert J., Dolag K., Lesch H., Müller E., 2009, *MNRAS*, **392**, 1008
- Doroshkevich A., Tucker D. L., Allam S., Way M. J., 2004, *A&A*, **418**, 7
- Driver S. P., et al., 2009, *Astronomy & Geophysics*, **50**, 5.12
- Farnes J. S., O'Sullivan S. P., Corrigan M. E., Gaensler B. M., 2014, *ApJ*, **795**, 63
- Feretti L., Dallacasa D., Giovannini G., Tagliani A., 1995, *Astronomy and Astrophysics*, **302**, 680
- Furlanetto S. R., Loeb A., 2001, *ApJ*, **556**, 619
- Gaensler B. M., 2009, in Strassmeier K. G., Kosovichev A. G., Beckman J. E., eds, IAU Symposium Vol. 259, Cosmic Magnetic Fields: From Planets, to Stars and Galaxies. pp 645–652 ([arXiv:0901.2952](https://arxiv.org/abs/0901.2952)), [doi:10.1017/S1743921309031470](https://doi.org/10.1017/S1743921309031470)
- Gaensler B. M., Landecker T. L., Taylor A. R., POSSUM Collaboration 2010, in American Astronomical Society Meeting Abstracts #215. p. 470.13
- Gilli R., et al., 2003, *ApJ*, **592**, 721
- Górski K. M., Hivon E., Banday A. J., Wand elt B. D., Hansen F. K., Reinecke M., Bartelmann M., 2005, *ApJ*, **622**, 759
- Grasso D., Rubinstein H., 1995, *Astroparticle Physics*, **3**, 95
- Grasso D., Rubinstein H. R., 2001, *Physics Reports*, **348**, 163
- Hambly N. C., et al., 2001, *MNRAS*, **326**, 1279
- Hammond A. M., Robshaw T., Gaensler B. M., 2012, arXiv e-prints, p. [arXiv:1209.1438](https://arxiv.org/abs/1209.1438)
- Heald G., 2009, *Cosmic Magnetic Fields: From Planets, to Stars and Galaxies*, **259**, 591
- Jarrett T., 2004, *Publ. Astron. Soc. Australia*, **21**, 396
- Kahniashvili T., Tevzadze A. G., Brandenburg A., Neronov A., 2013, *Phys. Rev. D*, **87**, 083007
- Kawasaki M., Kusakabe M., 2012, *Phys. Rev. D*, **86**, 063003
- Kim K. T., Kronberg P. P., Dewdney P. E., Landecker T. L., 1990, *ApJ*, **355**, 29
- Kim K. T., Tribble P. C., Kronberg P. P., 1991, *ApJ*, **379**, 80
- King I. R., 1972, *ApJ*, **174**, L123
- Klar J. S., Mücke J. P., 2012, *MNRAS*, **423**, 304
- Kolatt T., 1998, *ApJ*, **495**, 564
- Kopylova F. G., Kopylov A. I., 2013, *Astronomy Letters*, **39**, 1
- Kronberg P. P., 2016, Magnetic fields associated with clusters and groups of galaxies. Cambridge University Press, pp 162–191, [doi:10.1017/CBO9780511977657.010](https://doi.org/10.1017/CBO9780511977657.010)
- Kronberg P. P., Perry J. J., 1982, *ApJ*, **263**, 518
- Kronberg P. P., Lesch H., Hopp U., 1999, *The Astrophysical Journal*, **511**, 56
- Kronberg P. P., Bernet M. L., Miniati F., Lilly S. J., Short M. B., Higdon D. M., 2008, *ApJ*, **676**, 70
- Kulsrud R. M., Zweibel E. G., 2008, *Reports on Progress in Physics*, **71**, 046901
- Lan T.-W., Prochaska J. X., 2020, *MNRAS*, **496**, 3142
- Leahy J. P., 1987, *MNRAS*, **226**, 433
- Lee J., Pen U.-L., Taylor A. R., Stil J. M., Sunstrum C., 2009, arXiv e-prints, p. [arXiv:0906.1631v1](https://arxiv.org/abs/0906.1631v1)
- Lee J., Pen U.-L., Taylor A. R., Stil J. M., Sunstrum C., 2010, arXiv e-prints, p. [arXiv:0906.1631v2](https://arxiv.org/abs/0906.1631v2)
- Locatelli N., Vazza F., Bonafede A., Banfi S., Bernardi G., Gheller C., Botteon A., Shimwell T., 2021, arXiv e-prints, p. [arXiv:2101.06051](https://arxiv.org/abs/2101.06051)
- Ma Y. K., Mao S. A., Stil J., Basu A., West J., Heiles C., Hill A. S., Betti S. K., 2019a, *MNRAS*, **487**, 3432
- Ma Y. K., Mao S. A., Stil J., Basu A., West J., Heiles C., Hill A. S., Betti S. K., 2019b, *MNRAS*, **487**, 3454
- Madau P., Dickinson M., 2014, *ARA&A*, **52**, 415
- Man A., Belli S., 2018, *Nature Astronomy*, **2**, 695
- Mao S. A., et al., 2017, *Nature Astronomy*
- Neronov A., Semikoz D., Banafsheh M., 2013, arXiv e-prints, p. [arXiv:1305.1450](https://arxiv.org/abs/1305.1450)
- O'Sullivan S. P., et al., 2012, *MNRAS*, **421**, 3300
- O'Sullivan S. P., et al., 2019, *A&A*, **622**, A16
- O'Sullivan S. P., et al., 2020, *MNRAS*, **495**, 2607
- Oppermann N., et al., 2012, *A&A*, **542**, A93
- Oppermann N., et al., 2015, *A&A*, **575**
- Oren A. L., Wolfe A. M., 1995, *ApJ*, **445**, 624
- Oyaizu H., Lima M., Cunha C. E., Lin H., Frieman J., Sheldon E. S., 2008, *ApJ*, **674**, 768
- Planck Collaboration et al., 2016a, *A&A*, **594**, A13
- Planck Collaboration et al., 2016b, *A&A*, **594**, A19
- Planck Collaboration et al., 2016c, *A&A*, **594**, A27
- Prochaska J. X., Zheng Y., 2019, *MNRAS*, **485**, 648
- Pshirkov M. S., Tinyakov P. G., Urban F. R., 2016, *Phys. Rev. Lett.*, **116**, 191302
- Ratcliffe A., Shanks T., Broadbent A., Parker Q. A., Watson F. G., Oates A. P., Fong R., Collins C. A., 1996, *MNRAS*, **281**, L47
- Ravi V., et al., 2016, *Science*, **354**, 1249
- Roland J., 1981, *A&A*, **93**, 407

- Ryu D., Kang H., Cho J., Das S., 2008, *Science*, **320**, 909
- Schnitzeler D. H. F. M., 2010, *MNRAS*, **409**, L99
- Shimwell T. W., et al., 2019, *A&A*, **622**, A1
- Shull J. M., 2014, *ApJ*, **784**, 142
- Simard-Normandin M., Kronberg P. P., 1980, *ApJ*, **242**, 74
- Sokoloff D. D., Bykov A. A., Shukurov A., Berkhuijsen E. M., Beck R., Poezd A. D., 1998, *MNRAS*, **299**, 189
- Springel V., Frenk C. S., White S. D. M., 2006, *Nature*, **440**, 1137
- Stasyszyn F., Nuza S. E., Dolag K., Beck R., Donnert J., 2010, *MNRAS*, **408**, 684
- Stil J. M., Taylor A. R., Sunstrum C., 2011, *ApJ*, **726**, 4
- Stuardi C., et al., 2020, arXiv e-prints, p. [arXiv:2004.05169](https://arxiv.org/abs/2004.05169)
- Taylor A. R., Stil J. M., Sunstrum C., 2009, *ApJ*, **702**, 1230
- Tumlinson J., Peebles M. S., Werk J. K., 2017, *ARA&A*, **55**, 389
- Vacca V., et al., 2015, *Astronomy and Astrophysics*
- Vallée J. P., 1995, *Ap&SS*, **234**, 1
- Vallée J. P., 1997, *Fundamentals Cosmic Phys.*, **19**, 1
- Vallée J. P., 1998, *Fundamentals Cosmic Phys.*, **19**, 319
- Vallée J. P., 2004, *New Astron. Rev.*, **48**, 763
- Vazza F., Ferrari C., Bonafede A., Brügger M., Gheller C., Braun R., Brown S., 2015a, in *Advancing Astrophysics with the Square Kilometre Array (AASKA14)*, p. 97 ([arXiv:1501.00315](https://arxiv.org/abs/1501.00315))
- Vazza F., Ferrari C., Brügger M., Bonafede A., Gheller C., Wang P., 2015b, *A&A*, **580**, A119
- Vazza F., Brügger M., Gheller C., Hackstein S., Wittor D., Hinz P. M., 2017, *Classical and Quantum Gravity*, **34**
- Vernstrom T., Gaensler B. M., Brown S., Lenc E., Norris R. P., 2017, *MNRAS*, **467**, 4914
- Vernstrom T., Gaensler B. M., Rudnick L., Andernach H., 2019, *ApJ*, **878**, 92
- Vernstrom T., Heald G., Vazza F., Galvin T., West J., Locatelli N., Forngeno N., Pinetti E., 2021, arXiv e-prints, p. [arXiv:2101.09331](https://arxiv.org/abs/2101.09331)
- Wenger M., et al., 2000, *A&AS*, **143**, 9
- Widrow L. M., 2002, *Rev. Mod. Phys.*, **74**, 775
- Wilcots E., 2004, *New Astron. Rev.*, **48**, 1281
- Wolfe A. M., Lanzetta K. M., Oren A. L., 1992, *ApJ*, **388**, 17
- Wright E. L., et al., 2010, *AJ*, **140**, 1868
- Xu J., Han J. L., 2014, *MNRAS*, **442**, 3329
- Xu Y., Kronberg P. P., Habib S., Dufton Q. W., 2006, *The Astrophysical Journal*, **637**, 19
- Zonca A., Singer L., Lenz D., Reinecke M., Rosset C., Hivon E., Gorski K., 2019, *Journal of Open Source Software*, **4**, 1298

This paper has been typeset from a  $\text{\TeX}/\text{\LaTeX}$  file prepared by the author.